



Modification Mechanism and Uniaxial Fatigue Performances of A356.2 Alloy Treated by Al-Sr-La Composite Refinement-Modification Agent

Liang Chang¹ · Qingfeng Zhao¹ · Xingchuan Xia¹ · Yuming Ding¹ · Binxu Guo¹ · Jian Ding¹ · Ying Tang¹ · Zan Zhang² · Chong Li³ · Xiaomian Sun⁴ · Junjie Guo⁵ · Kaihong Song¹ · Yongchang Liu³

Received: 5 July 2021 / Revised: 10 August 2021 / Accepted: 22 October 2021 / Published online: 1 November 2021
© The Chinese Society for Metals (CSM) and Springer-Verlag GmbH Germany, part of Springer Nature 2021

Abstract

Modification mechanism and uniaxial fatigue properties of A356.2 alloy treated by Al-6Sr-7La and traditional Al-5Ti-1B/Al-10Sr (hereinafter refers to traditional treated alloy) were investigated by constant stress amplitude method. Microstructure, dislocation and Si twinning of the alloys were studied by thermal analysis, scanning electron microscopy (SEM) and transmission electron microscopy (TEM). The results showed that Al-6Sr-7La possesses better refining and modification effect than Al-5Ti-1B/Al-10Sr. Meanwhile, fatigue properties of the alloy treated by Al-6Sr-7La are higher than traditional treated alloy, and this is mainly owing to that Al-6Sr-7La treated alloy has more twins in eutectic Si and lower twin spacing. In addition, higher density of nanophases formed on twin faces and La-rich clusters appear at multiple twin intersections. Stacking faults and entrapped nanophases appeared on growing Si twin faces. Impurity induced twinning (IIT) mechanism and twin plane re-entrant edge (TPRE) mechanism are valid for eutectic Si which are important for mechanical optimization of A356.2 alloy.

Keywords A356.2 alloy · Al-6Sr-7La · Fatigue property · Eutectic Si · Twins

1 Introduction

With the development of science and technology, increasing comprehensive performances of aluminum alloy has been put forward [1, 2]. Due to its excellent overall performances and low cost, A356.2 alloy has been widely used in many engineering structural components such as automotive

wheels, engine mounts, steering knuckles and so on [3–5], where repeated alternating loads during service and fatigue failure of the alloys should not be ignored. Statistics results showed fatigue causes about 80% fractures of Al alloy structural components in recent decades, with sudden fractures accounting for most of them, causing huge economic losses [6–8].

Coarse lamellar or needle-like eutectic silicon and large grain size in unmodified A356.2 alloy have negative effect on its fatigue resistance [9, 10]. Therefore, in order to improve its comprehensive mechanical properties, refiners and modifiers are usually applied to improve morphology of eutectic silicon and reduce grain size [11, 12]. In general, appropriate amount of modifier (Al-10Sr) is used to transform needle-like or long strip of eutectic Si into fibrous. Al-5Ti-1B is usually used for grain refinement, but when Si content is higher than 5 wt%, its refining effect will be weakened which is called “Si-poisoning” [13–16]. Various attempts have been made to overcome Si-poisoning. One way is to increase the amount of Al-5Ti-1B, but this is an expensive solution [17]. Another method is to reduce the content of Ti in the alloy and researchers have developed some refiners with better effect, such as Al-3Ti-3B, Al-Ti-C, Al-Ti-C-B,

Available online at <http://link.springer.com/journal/40195>.

✉ Xingchuan Xia
xc_xia@hebut.edu.cn

✉ Zan Zhang
zhangzan0706@163.com

¹ School of Material Science and Engineering, Hebei University of Technology, Tianjin 300130, China

² College of Physics and Electronic Engineering, Xingtai University, Xingtai 054001, China

³ School of Material Science and Engineering, Tianjin University, Tianjin 300130, China

⁴ CITIC Dicastal Co. Ltd., Qin Huangdao 066011, China

⁵ Qinhuangdao WKW Automotive Parts Co., Ltd., Qin Huangdao 066011, China

Al-5Nb-B, Al-V-B, Al-Ti-Nb-B and so on. However, manufacturing process of these refiners is more complex and difficult [18–22]. In recent years, rare earth elements (such as Ce, Er, Eu, Y, Yb, La, Sc, Zr) show significant effects on refinement metamorphism and tensile properties of Al-Si alloys [23–25]. Compared with unmodified Al-Si-Mg alloy, aspect ratio of eutectic Si was significantly decreased and mechanical properties were improved both under as-cast and T6 conditions by adding 0.2 wt% of Al-6.5Ce-3.5La [26]. In addition, Zr can increase fatigue life and tensile strength of Al-Si-Cu-Mg alloys [13]. As described above, though rare earths have important effect on the mechanical properties, there is still a lack of its effect on uniaxial fatigue properties of Al-Si-Mg alloys.

Previously, Al-6Sr-7La composite refinement-modification agent was developed and its synergistic effect on microstructure and tensile properties of A356.2 alloy were investigated [27–29]. The results showed that Al-6Sr-7La possessed excellent refinement and modification effect which significantly increased tensile strength, yield strength and elongation of A356.2 alloy, indicating a potential highly efficient composite refinement-modification agent. However, up to date, its effect on fatigue properties of A356.2 alloy is still unclear and relevant research should be carried out from the perspective of practical applications. In this work, effect of Al-6Sr-7La on the modification mechanism of eutectic Si and fatigue fracture mechanism of A356.2 alloy were investigated, traditional Al-10Sr and Al-5Ti-1B master alloys were used for comparison.

2 Experimental

Commercially available A356.2 alloy, Al-10Sr and Al-5Ti-1B master alloys were used in this work. Pure aluminum (with the purity of 99.99 wt%), commercial Al-10Sr and Al-20La are used to prepare Al-6Sr-7La master alloy. Detailed preparation process can be obtained in previous work [27, 29], and brief descriptions are as follows: Firstly, polish Al-10Sr, Al-20La and pure Al to remove the oxide scale and then dry it after washing by deionized water. Secondly, melt pure aluminum in resistance furnace at 740 °C and remove the slag after holding for 20 min. Thirdly, add Al-10Sr into the melt and hold for 20 min and then remove slag after cleaning by high-purity argon and stirring the melt for 5 min. Fourthly, add Al-20La into the melt and hold for 20 min and then remove slag after cleaning by high-purity argon and stirring the melt for 5 min. Finally, cool the melt to 720 °C and then pour into a preheated permanent mold to obtain Al-6Sr-7La master alloy. It should be noted that high-purity argon gas was used throughout the process to avoid oxidation. After that, A356.2 alloy was melted at 730 °C and 0.5 wt% Al-6Sr-7La was used

for refinement and modification. For comparison, 0.2 wt% Al-10Sr and 0.2 wt% Al-5Ti-1B were used. Muffle furnace with temperature control accuracy of ± 1 °C was used for T6 heat treatment. Specimens treated by Al-6Sr-7La and traditional Al-5Ti-1B/Al-10Sr were solution treated at 540 °C for 180 min and then immediately quenched into 60 °C water, after that, specimens were aged at 175 °C for 8 h, and then, specimens were taken out and naturally cooled to room temperature.

Typical metallographic method was applied for microstructure observation and samples were gradually grinded and polished. The morphologies were observed by a scanning electron microscope (SEM, JEOL JSM-6510A) with accelerating voltage of 15 kV and working current of 60 μ A. To reveal the morphology of eutectic Si intuitively, some samples were deeply etched with 30 vol.% hydrochloric acid solution. Self-developed thermal analysis system with data acquisition, data analysis and data processing modules is used to obtain solidification curve of the alloy. K-type thermocouple with sensitivity of 0.05 °C and sampling frequency of 5 counts/s was used. The microstructures were observed by a transmission electron microscopy (TEM, FEI Tecnai G2 F30) with accelerating voltage of 200 kV. Samples for TEM observation were firstly cut into 300 μ m slices using EDM wire cutter, and samples for fatigue mechanism analysis were cut from 1 mm under the fracture surface. Then, slices were thinned to 40–50 μ m using sandpapers from coarse to fine, followed by punching into $\Phi 3$ mm disks using sample puncher and cleaning in ultrasonic cleaner for 1–2 min. After that, the disks were electrolytically double-jet thinned using a double-jet thinner (MTP-1A), using dry ice and ethanol to control the temperature at -30 °C. Double-jet electrolyte was 30 vol.% methanol nitrate solution. Then, ion thinning (Gatan 691) with voltage, current and incidence angle of ion beam 5 V, 0.5 mA and $\pm 3^\circ$ was used to increase thin zone area. Liquid nitrogen was used for cooling throughout the process.

Fatigue test was carried out on PWS-100 electrohydraulic servo fatigue tester, and fatigue specimens were processed according to GB/T15248-2008 (Fig. 1) at room temperature. Fatigue tests were performed using sine wave loading with stress ratio of $R = -1$ and frequency of 10 Hz, stress controlled with stress levels between 10 and 40% of tensile strength and stopped after specimens fractured. At least two fatigue specimens were used for each set of tests.

3 Results and Discussion

3.1 Fatigue Properties

Generally, $S-N$ curve is used to describe fatigue behavior of alloys under stress control, and it is usually expressed by

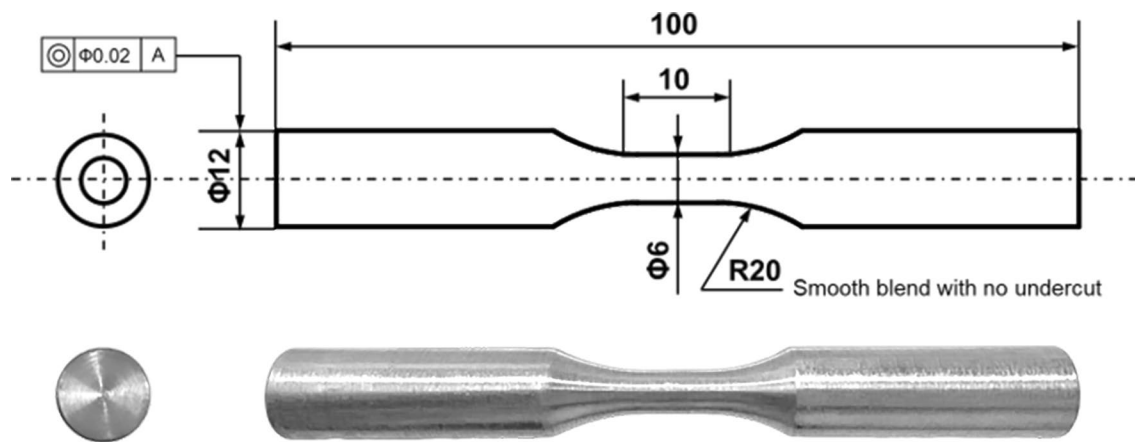


Fig. 1 Schematic and specimen for fatigue test

Basquin's equation which can reflect the trend of fatigue life with stress amplitude [6–8]:

$$\sigma_a = AN_f^b = (\sigma'_f \times 2^b) N_f^b, \quad (1)$$

where σ_a is stress amplitude, σ'_f is fatigue strength coefficient, N_f^b is the number of fatigue cycles, b denotes fatigue strength exponent. According to the data obtained from fatigue tests, specific values of fatigue parameters in Eq. (1) can be determined and a specific expression of relationship between applied stress amplitude and fatigue life can be obtained.

Figure 2 shows fatigue test results of controlled stresses performed during a pulling and pressing process at 10 Hz of load frequency. The fatigue properties of Al-6Sr-7La treated and traditional treated alloys were compared both under as-cast and T6 conditions. It can be seen that the fatigue life decreases gradually with the increase in stress amplitude both under as-cast and T6 conditions for

both of the two kinds of alloys. Under as-cast condition, fatigue life of Al-6Sr-7La treated alloy is obviously better than that of traditional treated alloy. Meanwhile, with the increase in stress amplitude, fatigue life difference between the two kinds of alloys shows a trend of gradually increasing. For instance, fatigue life of Al-6Sr-7La treated alloy is almost 2–4 times longer than that of traditional treated alloy when the stress amplitude is 180–200 MPa (Fig. 2a). Under T6 condition, fatigue life of Al-6Sr-7La treated alloy is obviously better than that of traditional treated alloy at lower stress amplitude. Especially when the stress is 240 MPa, fatigue life difference between the two alloys is the largest. However, fatigue life of the two alloys is almost the same at higher stress ranges. Overall, under the same stress amplitude, alloy treated by Al-6Sr-7La has longer fatigue period, meaning better fatigue resistance (Fig. 2b).

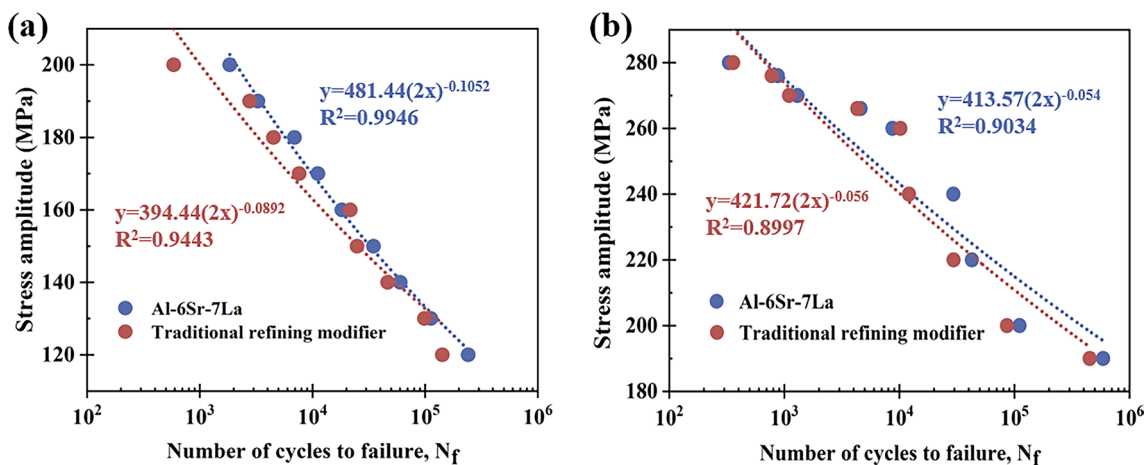


Fig. 2 S–N curves of A356.2 alloys under different conditions: **a** as-cast, **b** T6 treated

3.2 Cyclic Deformation Behavior

Figure 3 shows cyclic stress responses of T6 alloys treated by Al-5Ti-1B/Al-10Sr and Al-6Sr-7La, respectively, at different strain amplitudes. It is clear that cyclic stress response trends of the two kinds of alloys are more or less the same. Under lower cyclic stress amplitudes, maximum strain amplitude of the alloys decreases first and then increases with cycle number increasing, meaning cyclic hardening occurs first and then followed by cyclic softening until finally fatigue fracture. As for higher stress amplitudes, both alloys show continuous hardening on the first few cycles, and after a certain number of cycles instead of significant softening, it simply fractures. This is mainly due to that as stress amplitude rising, higher maximum strain results in larger slope at the beginning, meaning greater hardening rate of the alloy. In addition, more dislocation slip bands will initiate, making cyclic hardening more pronounced and fatigue fracture occurs before the alloy softening [7].

3.3 Evolution of Dislocation Configuration and Matrix Precipitates

Figure 4 shows 3D morphologies of eutectic Si under different conditions. For the unmodified alloy, coarse and massive eutectic Si aggregate together, which will severely deteriorate the strength and plasticity of the alloy [30] (Fig. 4a). As for the traditional treated alloy, though some coarse eutectic Si change to rod-like morphology, some massive and lamellar eutectic Si exist, further modification treatment is needed (Fig. 4b). As for the alloy treated by Al-6Sr-7La, refined fiber-like eutectic Si with uniform distribution indicates completely modified (Fig. 4c). Generally, morphology of eutectic Si and precipitates will influence fatigue life of alloys. As for unmodified alloy, coarse eutectic Si has strong splitting effect on the matrix and is easy to fall off from

the matrix, which will reduce fatigue life of the alloy. In addition, dislocations tend to accumulate at sharp corners or sharp edges of eutectic Si, which will significantly reduce its fatigue life. While for the alloy treated by Al-6Sr-7La, the splitting effect of fine eutectic Si on the matrix is weakened, and dislocation aggregation more evenly dispersed within eutectic zone which is beneficial to the improvement of fatigue properties [27].

Though modification treatment can optimize the morphology of eutectic Si, it can hardly change the distribution of eutectic Si which will cause uneven stress distribution easily during plastic deformation, resulting in dislocation enrichment and plugging near eutectic Si [8]. Figure 5 shows dislocation buildups around eutectic Si after different fatigue cycles. Almost no dislocation buildup can be found around eutectic Si before applying cyclic load (Fig. 5a). While, after certain cycles, large numbers of dislocations appear around eutectic Si and proliferate with fatigue cycles increasing. In addition, dislocation entanglement and buildup increase with the number of cycles (Fig. 5b and c).

Figure 6 shows representative dislocation distribution in the alloy treated by Al-6Sr-7La after different fatigue cycles. It is clear that density and proliferation of stress-induced dislocations are continuously increasing with cycle number increase which is responsible for the formation of more grain boundary cracks [4, 8]. After lower number of cycles, no obvious slip bands were formed (Fig. 6a). With increasing cycles, parallel slip bands appear, but these slip bands have strong discontinuities and larger spacing (Fig. 6b). After higher number of cycles, dislocations are severely packed and slip zone spacing is further reduced (Fig. 6c). Under higher cyclic stress amplitudes, fatigue life of the alloy is short, and the density of dislocations in the matrix is low. Some dislocations cannot cross grain boundaries, leading to cyclic hardening of alloys [6]. However, when dislocations build up to a certain level, dislocation arrays will form by

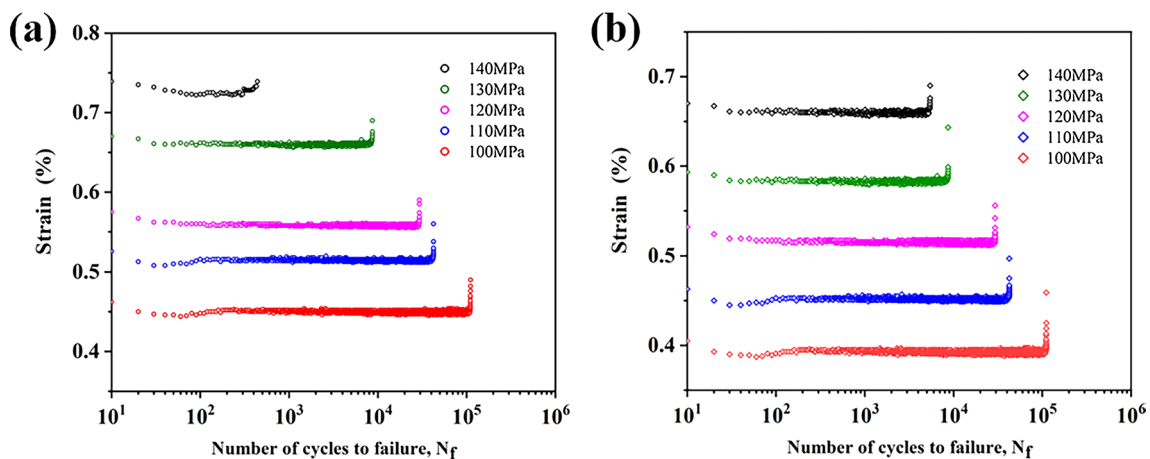


Fig. 3 Variation in cyclic strain amplitudes of T6 alloys treated by Al-5Ti-1B/Al-10Sr a, Al-6Sr-7La b

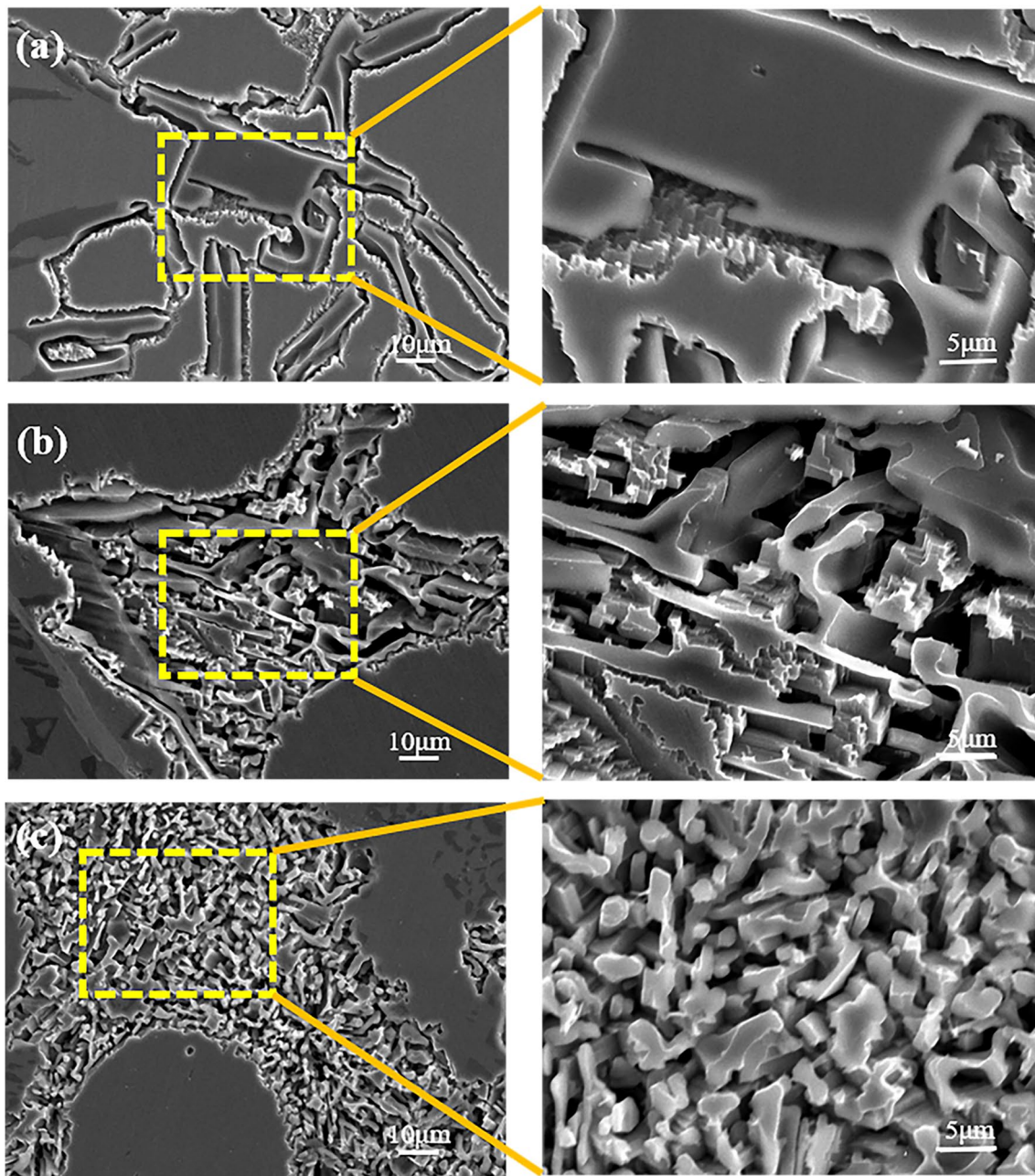


Fig. 4 Morphologies of eutectic Si extracted by deep etching **a** unmodified, **b** traditional treated alloy, **c** alloy treated by Al-6Sr-7La

dislocation reconfiguration which is responsible for cyclic softening [31–33] and this is consistent with the cyclic stress response behavior described in Fig. 3.

Besides eutectic Si morphology, initial microstructure is one important factor which will also affect fatigue behavior of alloys. Figure 7 shows bright-field TEM micrographs of the alloys (before fatigue test) treated by different refiners and modifiers. It is clear that under T6 conditions, a large number of diffusely distributed precipitated phases appear in both alloys with its density significantly higher in Al-6Sr-7La treated alloy compared with the traditional treated alloy,

which will increase dislocation impediment potential and improve fatigue properties of the alloy [8] (Fig. 7a and b). Figure 6c and d shows the high-resolution transmission electron microscopy (HRTEM), corresponding selected-area electron diffraction (SAED) and fast Fourier transformation (FFT) results of precipitated phase ($B = [001]_{Al}$). Two types of precipitated phases with spherical and short rod cross sections (Fig. 7c and d) were found. Based on FFT of HRTEM images, spherical and short rod-shaped precipitations were identified as Mg_2Si phase and Mg_5Si_6 phase, respectively, meaning that precipitation behavior within the matrix is

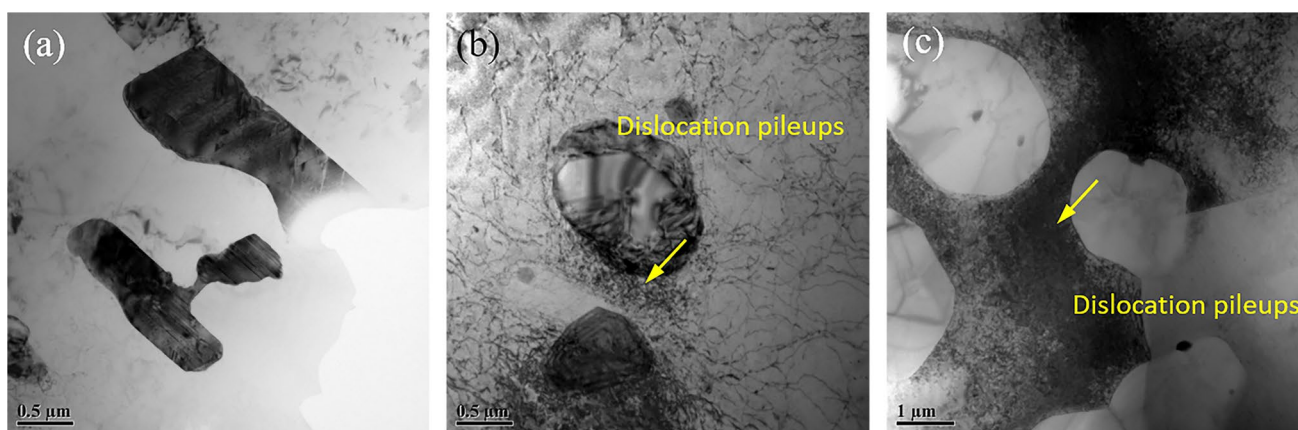


Fig. 5 Dislocation accumulation around eutectic Si **a** without cyclic loading, **b** after 6324 cycles, **c** after 110,441 cycles

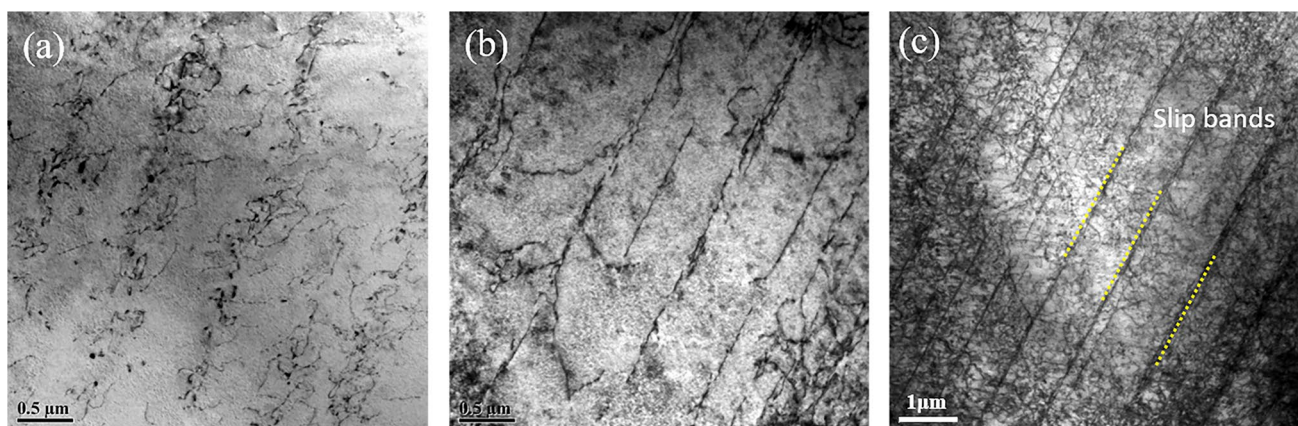


Fig. 6 Slip bands after different levels of cyclic fatigue deformation **a** after 6324 cycles; **b** after 34,851 cycles, **c** after 110,441 cycles

different from the eutectic area where Mg_2Si phase was not observed [27]. During the cyclic loading, in addition to the cracking of slip band, cracking of precipitated phase is also a kind of fatigue damage. Diffusely distributed precipitations have strong inhibitory effect on dislocation motion, making the activation energy of slip system near precipitated phases much higher and difficult to produce larger scale slip [8, 34].

3.4 Cooling Curves

Generally, solidification process can reflect a lot of useful information of alloy. To further clarify the refine and deterioration mechanism of Al-6Sr-7La, thermal analysis system was applied to obtain the cooling curves of the alloys. Figure 8 shows cooling curves of alloys (both treated by traditional Al-5Ti-1B/Al-10Sr and Al-6Sr-7La) by using a self-developed thermal analysis system. Corresponding characteristic temperatures are presented in Table 1. It can be seen that addition of refinement modifiers increases

the nucleation undercooling and all cooling curves exhibit marked recalescence. This is due to modifying elements may segregate in front of solid–liquid interface during the growth of eutectic Si, resulting in the increase in constitutional undercooling [35]. Under the present conditions, Al-6Sr-7La treated alloy has the lowest eutectic nucleation temperature (T_N) and eutectic growth temperature (T_G), and the highest recalescence temperature ($T_G - T_{min}$), which are 568.9 °C, 567.6 °C and 2.4 °C, respectively. Since lower eutectic nucleation temperature limits the nucleation of eutectic Si, lower eutectic growth temperature limits the growth rate of eutectic Si, thereby reducing the size of eutectic Si. It is generally believed that modification element modifies eutectic Si by inhibiting its growth [2, 23]. However, the effect of undercooling degree on the nucleation of eutectic Si is not fully considered. As we all know, undercooling degree is an important factor which will affect the nucleation and growth of eutectic Si. Studies have shown that nucleation undercooling degree has an important impact on the size

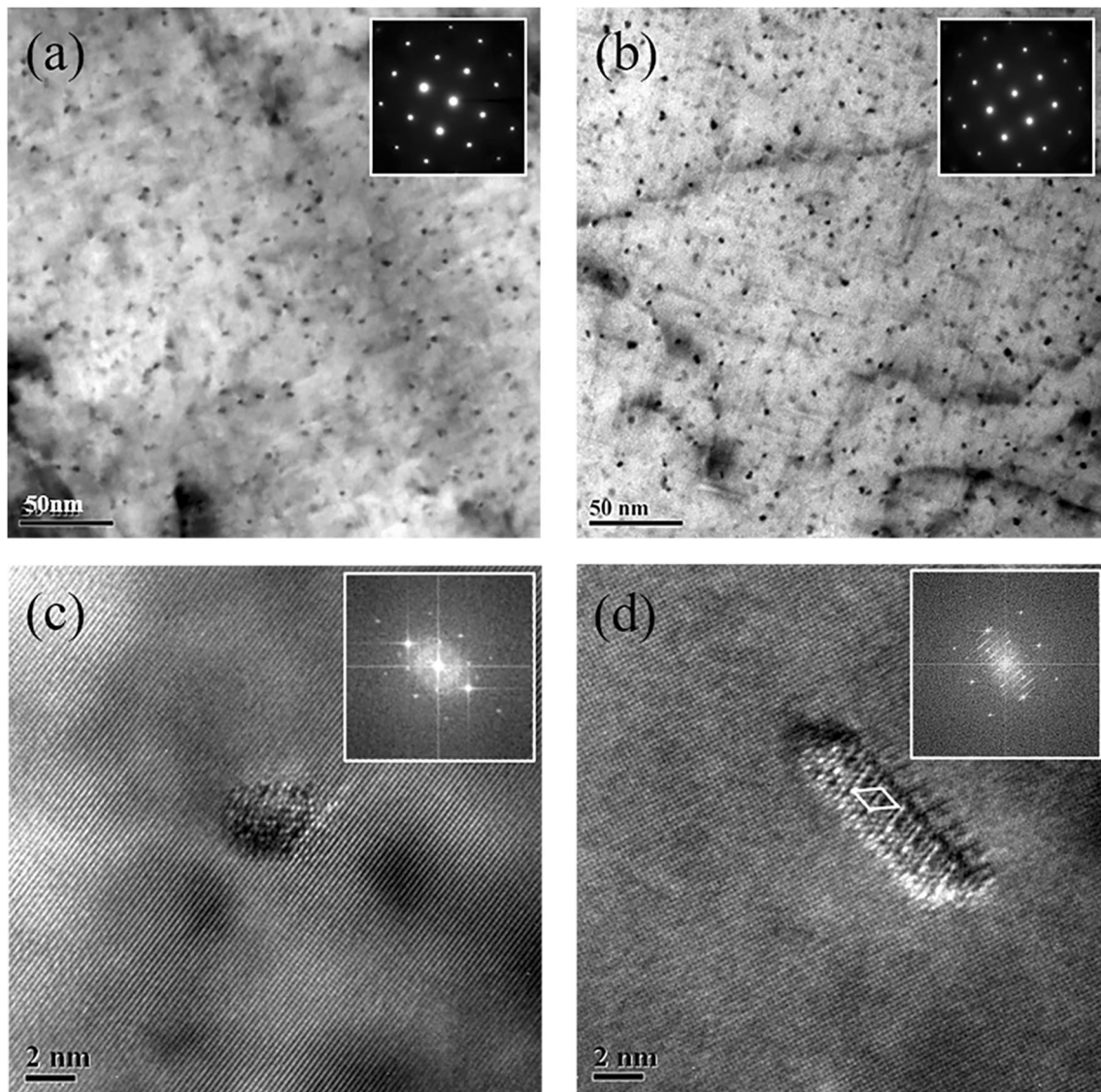


Fig. 7 Precipitates in traditional treated alloy **a** and Al-6Sr-7La treated alloy **b**, HRTEM of spherical cross section **c** and short rod-like cross section **d**

and morphology of eutectic Si, and when the undercooling is sufficient, morphology of eutectic Si will change [36]. However, the increase in undercooling degree caused by Al-6Sr-7La is still small, which is not enough to cause the morphology of eutectic Si transform from lamellar to fibrous. Therefore, increase in nucleation undercooling degree can only reduce the size of eutectic Si [37, 38].

3.5 Characteristics of Eutectic Si

In order to further explore modification mechanism of eutectic Si morphology, internal characteristics of eutectic Si were observed by TEM. Figure 9 shows the morphology of eutectic Si in the traditional treated alloy and Al-6Sr-7La

treated alloy with incident axis of $\langle 001 \rangle$. Twins appear in both alloys with growth twins spacing of about 30 nm in the traditional treated alloy and more growth twins with spacing of about 17 nm can be found in the Al-6Sr-7La treated alloy. Up to date, many researchers focus on modification mechanism of eutectic Si in Al-Si alloys [39–41] and there are two mechanisms currently accepted, namely TPPE (twin plane re-entrant edge) and IIT (impurity induced twinning). TPPE mechanism mainly considers the intersection of $\{111\}_{\text{Si}}$ twinning planes with the outer surface of Si crystal to produce concave angles which act as favorable locations for atomic adhesion and crystal growth. Si crystals preferentially grow along the direction of $\langle 112 \rangle$, and its growth can be hindered by adsorption of individual modified atoms

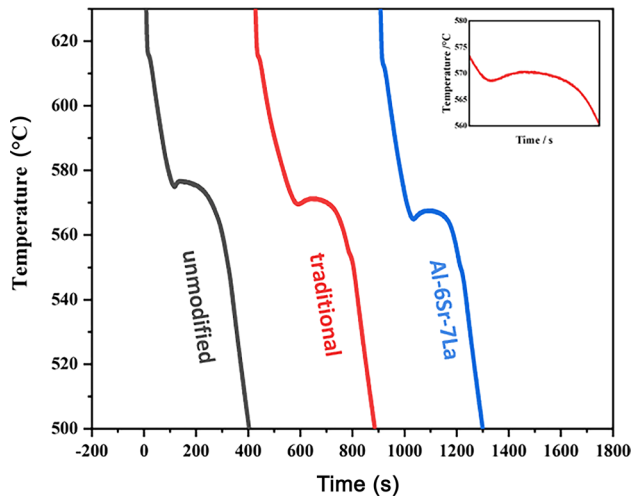


Fig. 8 Typical cooling curves of the alloys treated by different refiners and modifiers

Table 1 Characteristic temperatures of the alloys

Alloy	T_N (°C)	T_{min} (°C)	T_G (°C)	$T_G - T_{min}$ (°C)
Unmodified	577.8	575.4	576.8	1.4
Traditional	571.4	569.1	571.2	2.1
Al-6Sr-7La	568.9	565.2	567.6	2.4

at TPRES, resulting in the preferential growth of Si is eliminated. As for IIT mechanism, a radius ratio of ($r/r_{Si} = 1.646$) is proposed as ideal value of modifier atoms to Si atoms and the modifier atoms can promote high-density Si twins on

$\{111\}_{Si}$ planes. Based on this, there are growth twins in both alloys, indicating that TPRES mechanism is effective [40].

Figure 10 shows HRTRM results of multi-twin along $\langle 112 \rangle$ Si growth direction and the twins mainly grow along two directions (Fig. 10a) with the angle of 70.5° [24]. At the intersection of two $\{111\}_{Si}$, La-rich Al-Si-La clusters appear (Fig. 10c). In addition, no significant La concentration was found in other defect-free region and it is speculated that La tends to at the twin intersection of eutectic Si. Preferential adsorption of La atoms along twin boundaries prevents the preferential growth of Si in TPRES. La-rich clusters can make eutectic Si grow from one $\{111\}_{Si}$ plane to another $\{111\}_{Si}$ plane. By continuously changing growth direction, high-density parallel twins and cross twins can be induced, so that the morphology of eutectic Si changes from lamellar to fibrous [41]. Besides, as the growth of twins, La atoms incorporate into TPRES column, demonstrating that TPRES poisoning mechanism and IIT mechanism are also effective for eutectic Si, similar phenomenon was also reported in other Al-Si alloys [39–42].

However, only TPRES mechanism and IIT mechanism cannot fully explain the transition mechanism of eutectic Si from plate-like to fine fibrous in Al-6Sr-7La treated alloy. Figure 11 shows a typical TEM photograph of eutectic Si in Al-6Sr-7La treated alloy. It is clear in Fig. 11a that multiple directional twins appear in eutectic Si and under higher magnification dark-field condition high density of nanoparticles distributed in eutectic Si (Fig. 11b and c). Meanwhile, some scattered nanoparticles are also found between the twins in different directions. These nanoparticles can not only promote uneven nucleation of eutectic Si, but also prevent its growth, resulting in its modification.

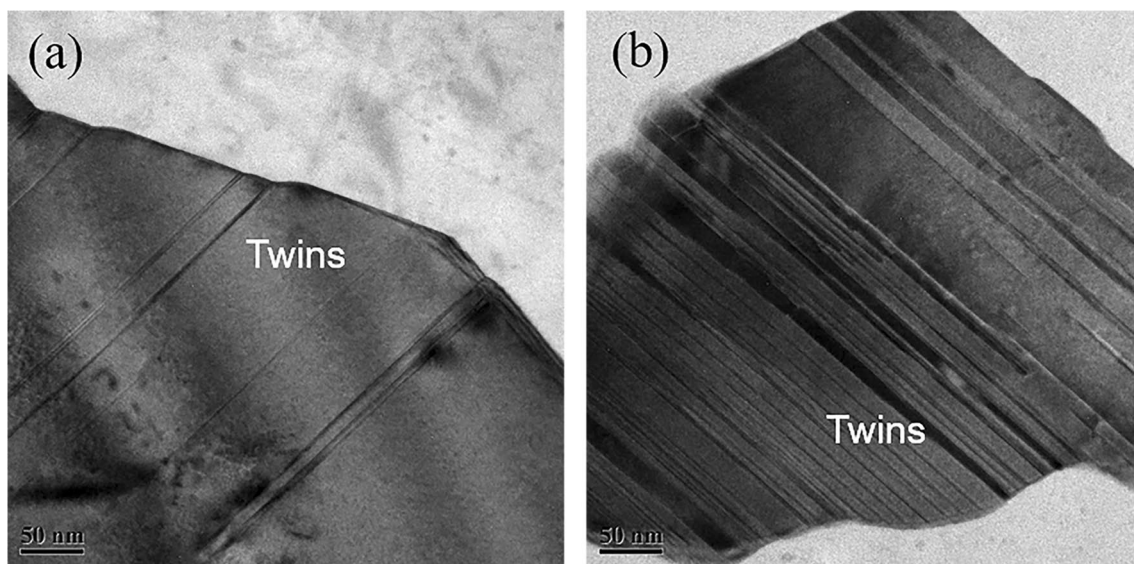


Fig. 9 Eutectic Si in traditional treated **a**, Al-6Sr-7La treated **b** alloys

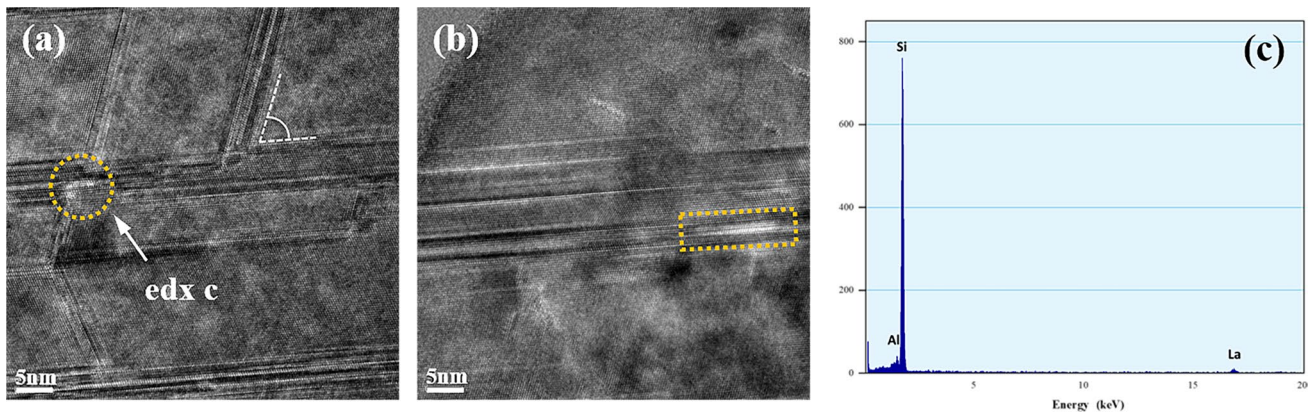


Fig. 10 a, b HRTEM results of intersecting twins in eutectic Si, c EDX analysis

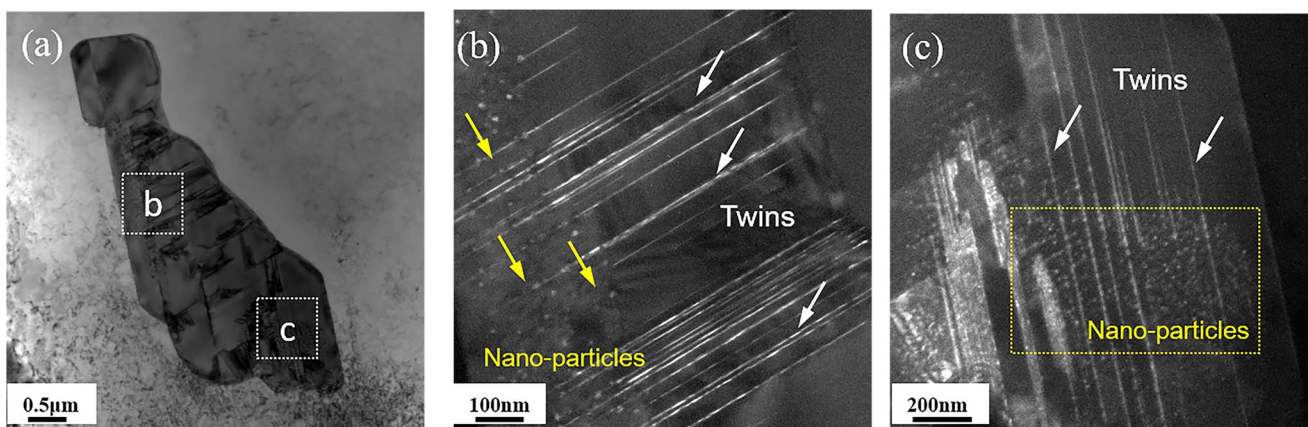


Fig. 11 Al-6Sr-7La treated alloy: a overall morphology of eutectic Si, b c dark-field images of corresponding area in a at higher magnification

According to TPPE mechanism and IIT mechanism, adsorption single modification atom at twin boundary or growth plane will hinder the growth of eutectic Si [39, 43]. However, it is not only modification atoms that hinder the growth of eutectic Si, but also nanoparticles.

In addition, “bean-petal” shape particles with its dimensions of about 200 nm appear in eutectic silicon (Fig. 12). High-density twins and a large number of internal stacking faults are found “bean-petal” shape particles, leading to the elongation of diffraction spot [32, 34] (Fig. 12c and d). Generally, Si has low stacking fault energy and is prone to forming stacking fault, however, stacking fault and kink were only observed in Al-6Sr-7La treated alloy. Meanwhile, kink consists of multiple tilted small angle grain boundaries (SAGBs), which are parallel to each other, and constant orientation difference angle is created on either side of kink, resulting in the different orientation of eutectic Si. Furthermore, accumulation of kink and stacking fault will result in larger strain and increase the orientation difference in $\langle 112 \rangle_{\text{Si}}$ direction, leading to the

anisotropic growth of eutectic Si and ultimately change its morphology.

3.6 Fracture Characteristics

Figure 13 shows representative fractography of Al-6Sr-7La treated alloy with stress amplitudes of 180 MPa. Three distinct zones were clearly distinguished, including fatigue crack initiation (FCI) zone, fatigue crack growth (FCG) zone and final fracture (FF) zone which are in good agreement with high cycle fatigue fracture morphology [13]. Figure 13b and c shows crack initiated exclusively from shrinkage pores. Generally, pores in alloy have detrimental effect on fatigue performance especially in large quantities, large size and complex shapes which will result in high stress/strain concentrations near the porosity. When the number and size of pores are controlled below a critical level, oxide inclusions will become the next main influencing factors.

Figure 14 shows sources of fatigue crack initiation in the alloy under different stress amplitudes. It is clear that

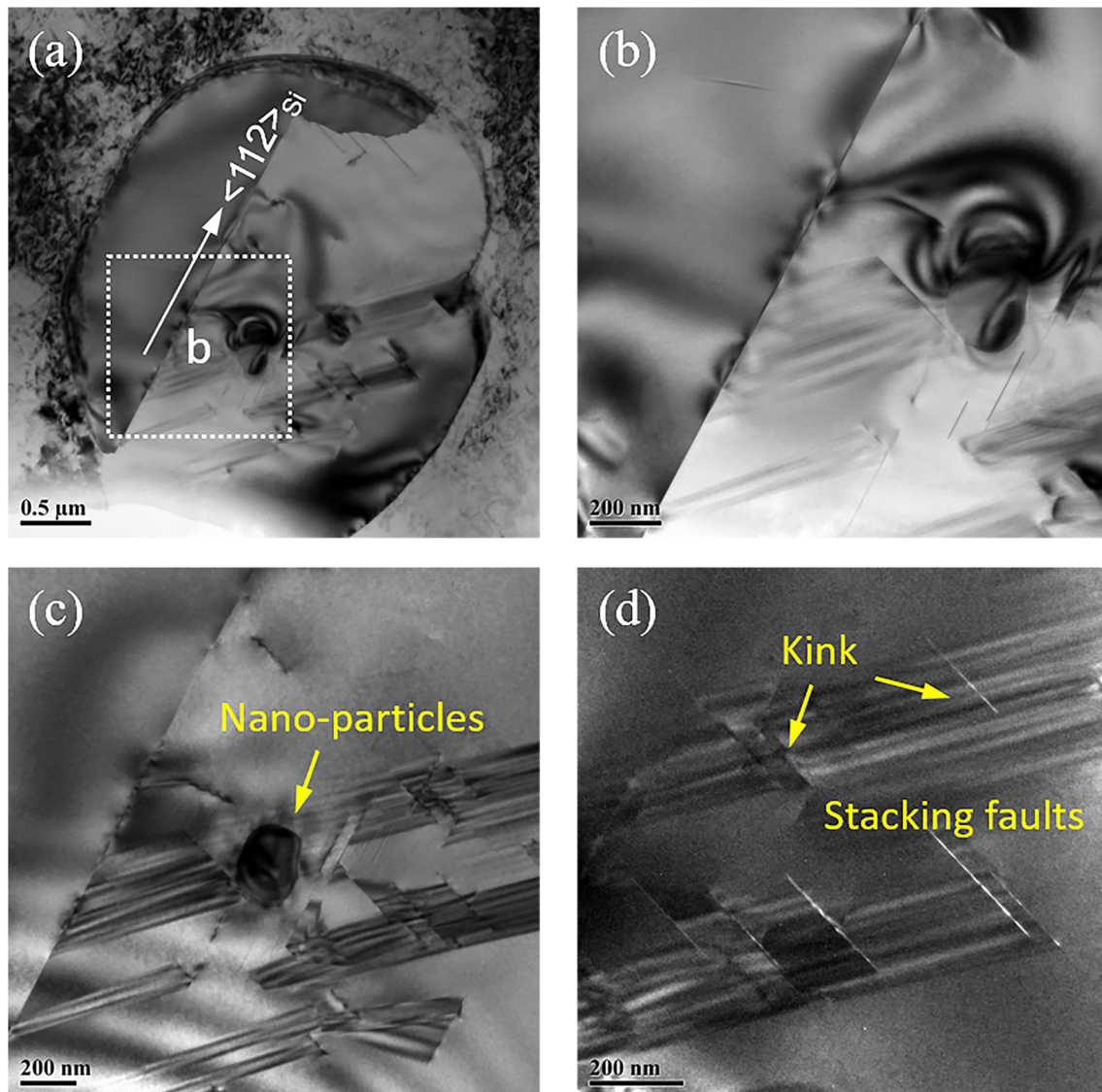


Fig. 12 Bright-field TEM images of Al-6Sr-7La modified alloy: **a** overall morphology of eutectic Si, **b** corresponding area in **a** at higher magnification, **c** nanoparticles, **d** stacking faults

when stress level is below the yield point of the alloy, fatigue cracking mainly associates with defects, such as internal inclusions and surface machining defects. Based on energy dispersive spectroscopy (EDS) results and its dimensions, inclusions should be primary oxidation inclusions formed during melting and casting processes (Fig. 14a). At this time, the fatigue source area is circular on the fracture and many secondary cracks around the inclusions appear which are mostly due to the breaking away of inclusions or eutectic Si from the matrix [44] (Fig. 14b). In addition, unfused pores present both on the surface and inside of the specimen, and fatigue cracks initiating from pores expand during early expansion process in the form of grain-piercing fractures, while the crack expansion path was altered during expansion

due to the obstruction of eutectic Si, resulting in a radial pattern (Fig. 14c and d). It is generally accepted that porosity, inclusions, eutectic Si and iron-rich equivalents all will cause stress concentrations and decrease plastic deformation ability of the alloy under cyclic fatigue loading, resulting in cracking. From the fracture morphology, it can be found that there are different priorities as fatigue crack sources [7, 13]. Under large stress amplitude, pores are more likely to be the fatigue crack source due to its complex spatial morphology, and fatigue crack is more likely initiates at the tips or protrusions of pores. Under small stress amplitude, oxide inclusion is more likely to be crack source.

Under higher magnification of FCG zone (Fig. 15), related to $\langle 110 \rangle_{Al}$ axis and dislocation walls, regular fatigue

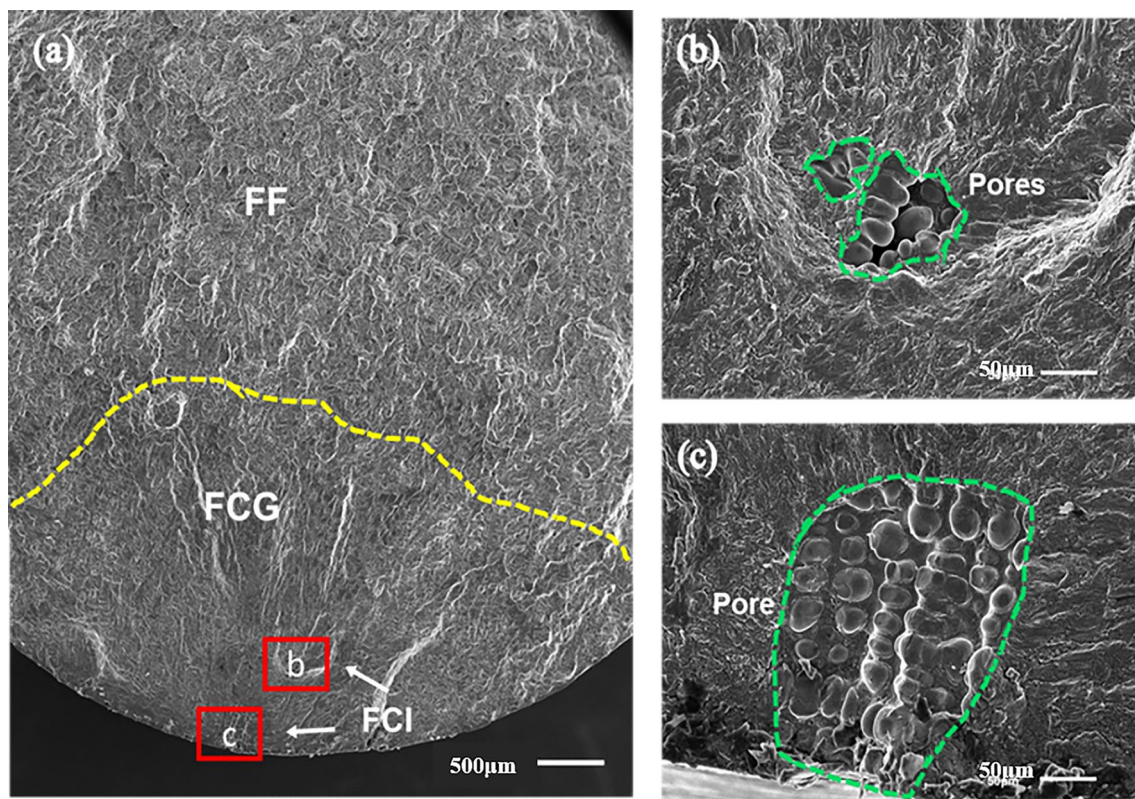


Fig. 13 a Fatigue fracture surface under stress amplitudes of 180 MPa, b c crack initiation

striations appear which are typical microscopic feature in stable extension phase of fatigue cracks. It is clear that fatigue striations are parallel to each other and perpendicular to crack expansion direction. In addition, fatigue striation is blunt undulating pattern which is caused by repeated opening and closing of plastic deformation zone at the tip of fatigue cracks. Meanwhile, formation of fatigue cracks is also accompanied by static fracture phenomena, such as the dents and splits in Fig. 14a. Also, fatigue striations width gradually decreases as fatigue life increases with decreasing stress amplitude [31, 42]. With the fatigue crack expansion rate decreasing under low cyclic stress, fatigue striations density increases with the distance between two adjacent fatigue striations approximately 0.5 μm after 110,441 cycles, while the distance between two adjacent fatigue striations being approximately 1.9 μm after 6324 cycles with more secondary cracks. Generally, each striation line represents a deformation cycle, the numbers of fatigue cycle and striation is theoretically the same, but the statistics show that the number of fatigue glow lines is much smaller than corresponding fatigue cycles. This is because fatigue fretting generally occurs only in FCG zone and mainly in the weak areas of the alloy. When fatigue cracks encounter large second-phase particles (such as iron-rich equivalents) during

their extension, they will bypass the second-phase particles and continue propagating [44, 45].

Figure 16a shows crack extension zone at the stress amplitude of 130 MPa. It can be seen that at lower stress amplitudes, mainly eutectic Si fracture occurs, while at higher stress amplitudes of 280 MPa (Fig. 16b), besides eutectic fracture most needle-like iron-rich phases involve in crack extension, meaning that stress amplitude significantly influences fatigue crack extension behavior [46–48]. In general, needle-like $\beta\text{-Al}_5\text{FeSi}$ phase has the most detrimental effect on the mechanical properties of Al alloys [49–51]. Figure 17 shows needle-like iron-rich phase ($\beta\text{-Al}_5\text{FeSi}$) which is distributed on the grain boundaries with monoclinic crystal structure. Under stress loading conditions, plastic strain energy is sufficient to cause $\beta\text{-Al}_5\text{FeSi}$ debond from $\alpha\text{-Al}$ matrix and micro-pores formed by debonding will lead to the fracture of the alloy [6, 51].

4 Conclusions

In this work, Al-6Sr-7La was used to composite refine and modify A356.2 alloy. Modification mechanism of Al-6Sr-7La and its effect on the uniaxial fatigue fracture behavior

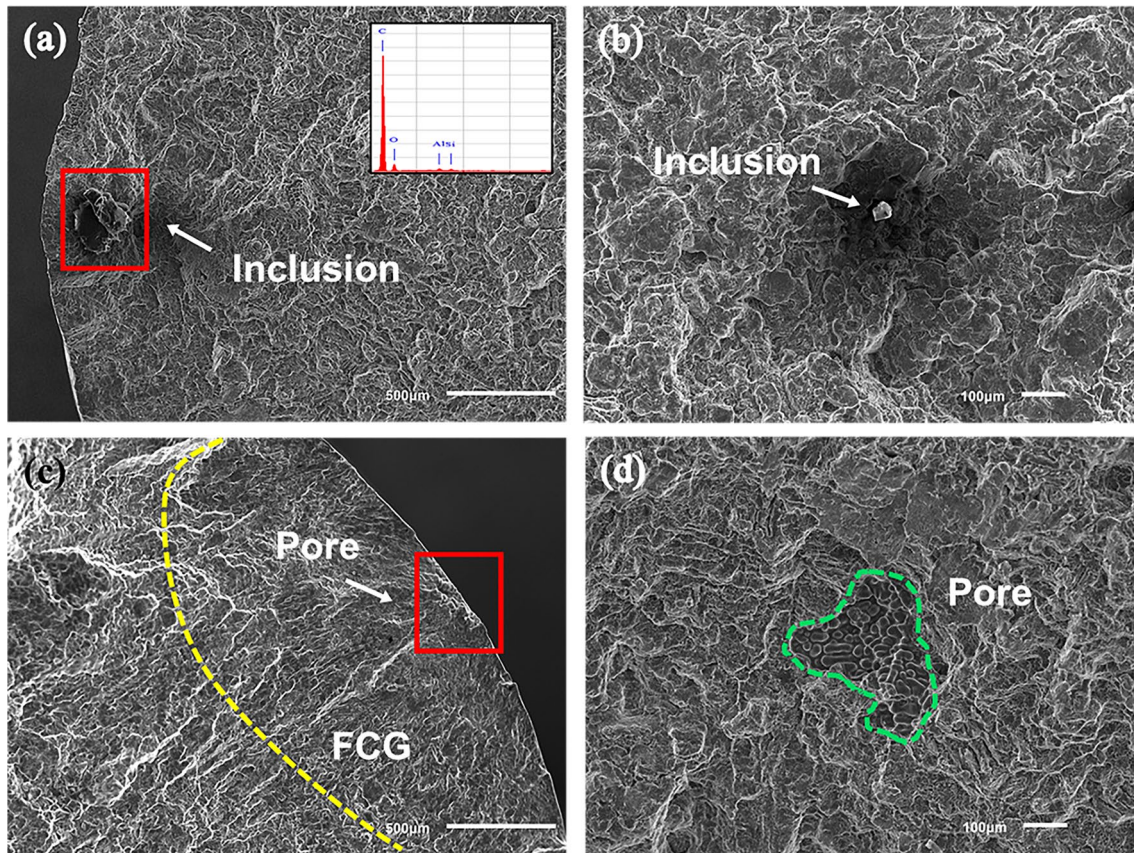


Fig. 14 Fatigue crack initiation: **a** surface inclusions, **b** internal inclusions, **c** surface pores, **d** internal pores

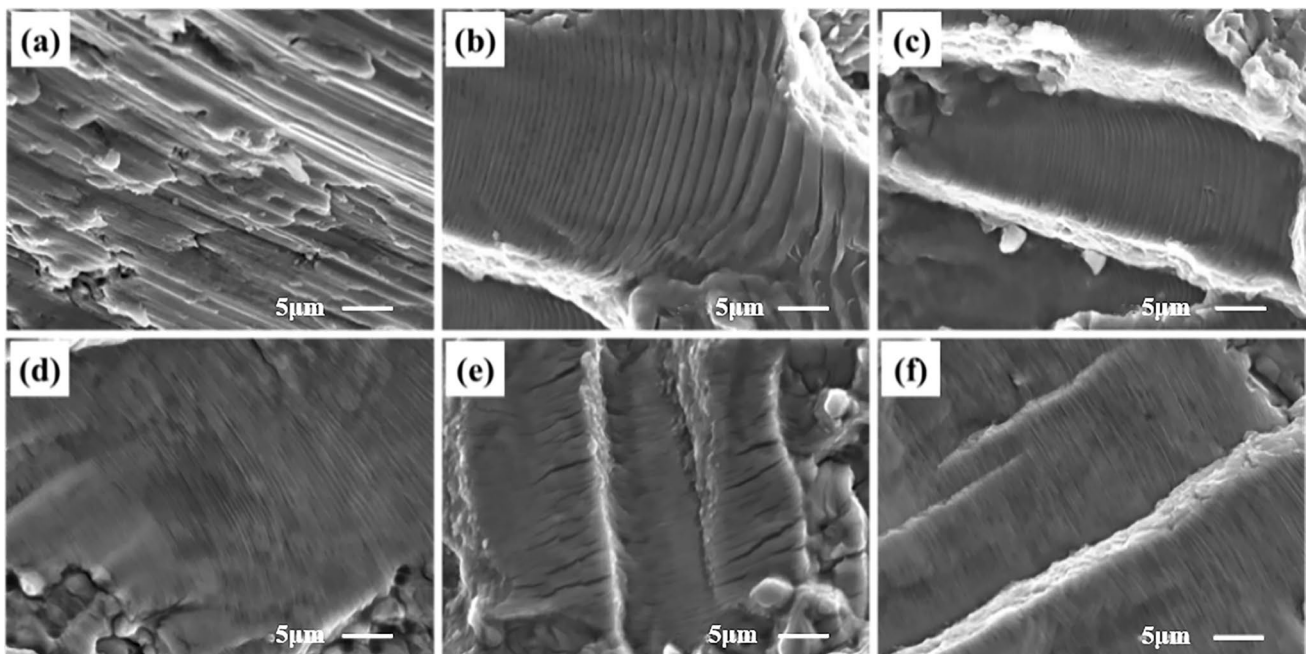


Fig. 15 Fatigue striations in the alloys after different cycles: **a** 6324, **b** 24,931, **c** 34,851, **d** 60,123, **e** 87,263, **f** 110,441

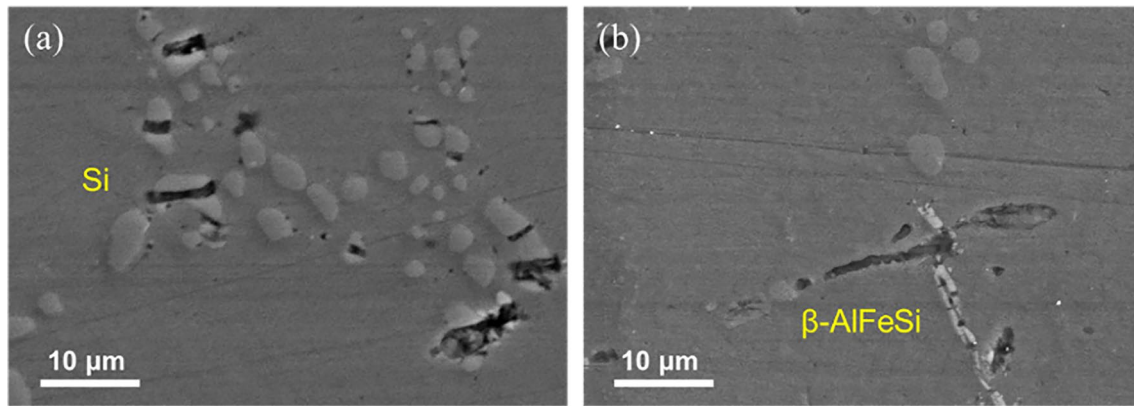


Fig. 16 Fractured **a** eutectic Si, **b** iron-rich phase in FCG zone

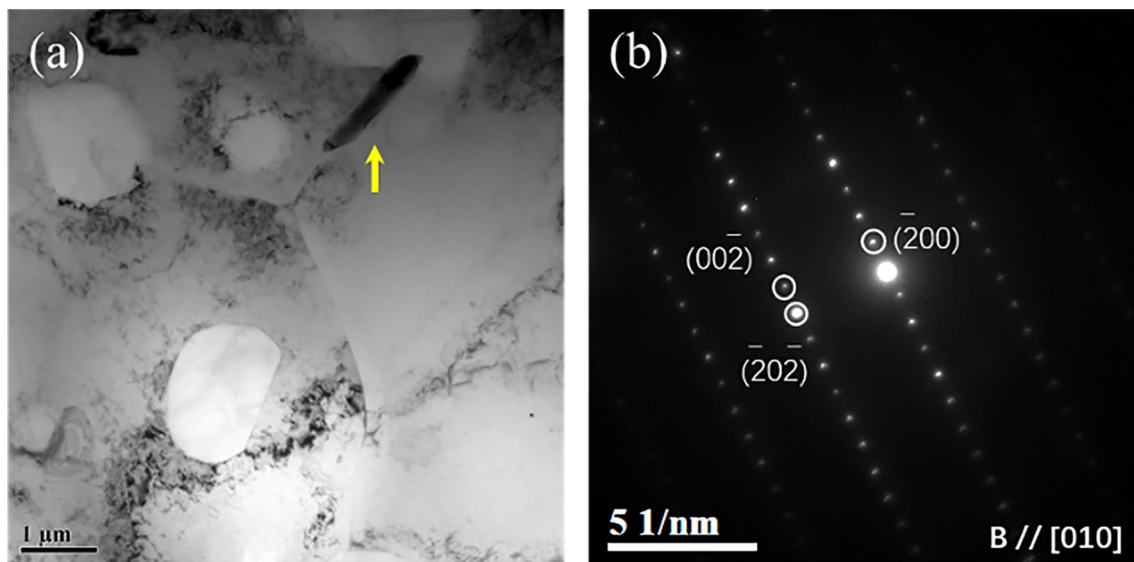


Fig. 17 **a** TEM image of iron-rich phase, **b** SAED results

of the alloy were investigated. Based on the experimental results, conclusions are summarized as follows.

1. Compared with traditional Al-5Ti-1B/Al-10Sr, Al-6Sr-7La master alloy can cause greater constitutional undercooling, more twins and precipitated phases are produced in eutectic Si. In addition, refinement and modification effect of Al-6Sr-7La is significantly better than traditional Al-5Ti-1B/Al-10Sr.
2. Increasing of constitutional undercooling caused by Al-6Sr-7La reduces the size of eutectic Si by suppressing its nucleation. La-rich clusters and nanophases in eutectic Si can change the morphology of eutectic Si by inhibiting its growth and inducing high-density twins.
3. Improvement of eutectic Si modification and precipitation of Mg_2Si and Mg_5Si_6 phases improve fatigue resist-

ance of the Al-6Sr-7La treated alloy. Fatigue loading leads to dislocation entanglement and aggregation which is beneficial to form dislocation lines.

4. Fatigue cracks mainly initiate from pores and inclusions, and pores have higher priority as crack sources under larger stress amplitude. Oxidation inclusions are more likely to act as crack sources when the stress amplitude is lower.

Acknowledgements This work was financially supported by the National Key R&D Program of China (Grant No. 2018YFB2001800), the Military-civilian integration project of Hebei Province, Provincial School Cooperation Fund of Hebei province, Key R&D Program of Hebei Province (No. 19251013D) and the Natural Science Foundation of Hebei Province (Nos. E2019202161 and E2021202091).

Declarations

Conflict of interest The authors state that there are no conflicts of interest to disclose.

References

- [1] W.M. Jiang, J.W. Zhu, G.Y. Li, F. Guan, Y. Yu, Z.T. Fan, *J. Mater. Sci. Technol.* **88**, 119 (2021)
- [2] J.W. Zhu, W.M. Jiang, G.Y. Li, F. Guan, Y. Yu, Z.T. Fan, *J. Mater. Process. Technol.* **283**, 116699 (2020)
- [3] G. Rana, J.E. Zhou, Q.G. Wang, *J. Mater. Process. Technol.* **207**, 1 (2008)
- [4] W.Y. Liu, W.L. Xiao, C. Xu, M.W. Liu, C.L. Ma, *Mater. Sci. Eng. A* **693**, 93 (2017)
- [5] X.R. Liu, Y.D. Zhang, B. Beausir, F. Liu, C. Esling, F.X. Yu, X. Zhao, L. Zuo, *Acta Mater.* **97**, 338 (2015)
- [6] K. Hu, C.H. Lin, S.C. Xia, C.K. Zheng, B. Lin, *Mater. Charact.* **170**, 110680 (2020)
- [7] J.Z. Yi, Y.X. Gao, P.D. Lee, T.C. Lindley, *Metall. Mater. Trans. B* **37**, 2 (2006)
- [8] T. Haskel, G.O. Verran, R. Barbieri, *Int. J. Fatigue* **114**, 1 (2018)
- [9] H.R. Zhang, Z.B. Liu, Z.Z. Li, G.W. Li, H. Zhang, *Acta Metall. Sin. Engl. Lett.* **29**, 414 (2016)
- [10] Z. Liu, W.M. Mao, Z.D. Zhao, *Acta Metall. Sin. Engl. Lett.* **21**, 1 (2008)
- [11] Y.J. Shi, L.J. Liu, L. Zhang, L.J. Zhang, L. Zheng, R.X. Li, B.Y. Yu, *J. Iron Steel Res. Int.* **24**, 9 (2017)
- [12] D. Han, Y.J. Zhang, X.W. Li, *Acta Mater.* **205**, 116559 (2021)
- [13] G.Y. Liu, P. Blake, S.X. Ji, *J. Alloys Compd.* **809**, 151795 (2019)
- [14] Y. Li, Y. Jiang, B. Hu, Q. Li, *Scr. Mater.* **187**, 262 (2020)
- [15] Y. Li, B. Hu, B. Liu, A.M. Nie, Q.F. Gu, J.F. Wang, Q. Li, *Acta Mater.* **187**, 51 (2020)
- [16] H. Yu, N. Wang, R.G. Guan, D. Tie, Z. Li, Y.A. An, Y. Zhang, *J. Mater. Sci. Technol.* **34**, 2297 (2018)
- [17] H.C. Liao, G.X. Sun, *Scr. Mater.* **48**, 8 (2003)
- [18] D. Qiu, J.A. Taylor, M.X. Zhang, P.M. Kelly, *Acta Mater.* **55**, 4 (2007)
- [19] Y. Li, Y. Jiang, B. Liu, Q. Luo, B. Hu, Q. Li, *J. Mater. Sci. Technol.* **65**, 6 (2021)
- [20] L.Y. Liu, T. Gao, K. Zhao, X.F. Liu, *Mater. Lett.* **288**, 129367 (2021)
- [21] K. Zhao, T. Gao, H.B. Yang, G.L. Liu, Q.Q. Sun, C.C. Wu, J.F. Nie, X.F. Liu, *J. Alloys Compd.* **820**, 153089 (2020)
- [22] J. Xu, Y. Li, K. Ma, Y.A. Fu, E.Y. Guo, Z.N. Chen, Q.F. Gu, Y.X. Han, T.M. Wang, Q. Li, *Scr. Mater.* **187**, 142 (2020)
- [23] Y. He, H.H. Xi, W.Q. Ming, Q.Q. Shao, R.H. Shen, Y.X. Lai, C.L. Wu, J.H. Chen, *Trans. Nonferr. Met. Soc. China* **31**, 1 (2021)
- [24] F. Mao, S.Z. Wei, C. Chen, C. Zhang, X.D. Wang, Z.Q. Cao, *Mater. Des.* **186**, 108268 (2020)
- [25] B.B. Yu, H. Yan, J.B. Zhu, J.L. Liu, H.G. Li, Q. Nie, *Acta Metall. Sin. Engl. Lett.* **32**, 443 (2019)
- [26] W.M. Jiang, Z.T. Fan, Y.C. Dai, C. Li, *Mater. Sci. Eng. A* **597**, 237 (2014)
- [27] X.C. Xia, Q.F. Zhao, Y.Y. Peng, P. Zhang, L.H. Liu, J. Ding, X.D. Luo, L.S. Wang, L.X. Huang, H.J. Zhang, X.G. Chen, *J. Alloys Compd.* **818**, 153370 (2020)
- [28] J. Ding, S.N. Miao, B.J. Ma, X.C. Xia, C.R. Qiu, X.G. Chen, *Adv. Eng. Mater.* **20**, 6 (2018)
- [29] C.R. Qiu, S.N. Miao, X.R. Li, X.C. Xia, J. Ding, Y.N. Wang, W.M. Zhao, *Mater. Des.* **114**, 563 (2017)
- [30] Y.D. Jia, F.Y. Cao, P. Ma, J.S. Liu, J.F. Sun, G. Wang, *J. Iron Steel Res. Int.* **23**, 1 (2016)
- [31] C. Kienl, F.D. Leon-Cazares, C.M.F. Rae, *Acta Mater.* **000**, 115743 (2020)
- [32] B. Wang, P. Zhang, Q.Q. Duan, Z.J. Zhang, H.J. Yang, X.W. Lia, Z.F. Zhang, *Mater. Sci. Eng. A* **707**, 674 (2017)
- [33] J. Li, R. Ding, Q.Y. Guo, C. Li, Y.C. Liu, Z.M. Wang, H.J. Li, C.X. Liu, *Mater. Sci. Eng. A* **812**, 141113 (2021)
- [34] C.W. Shao, F. Shi, X.W. Li, *Mater. Sci. Eng. A* **667**, 208 (2016)
- [35] K.M. Amin, N.A. Mufti, *J. Mater. Process. Technol.* **212**, 8 (2012)
- [36] G. Heiberg, K. Nogita, A.K. Dahle, L. Arnberg, *Acta Mater.* **50**, 10 (2002)
- [37] G.L. Mao, H. Yan, C.C. Zhu, Z. Wu, W.L. Gao, *J. Alloys Compd.* **806**, 909 (2019)
- [38] L.F. Li, D.Q. Li, F. Mao, J. Feng, Y.Z. Zhang, Y.L. Kang, *J. Alloys Compd.* **826**, 154206 (2020)
- [39] S.Z. Lu, A. Hellawell, *Metall. Mater. Trans. A* **18**, 10 (1987)
- [40] M. Shamsuzzoha, L.M. Hogan, *Philos. Mag. A* **54**, 4 (1986)
- [41] K. Nogita, J. Drennan, A.K. Dahle, *Mater. Trans.* **44**, 4 (2003)
- [42] G.V. Prasad Reddy, P.M. Dinesh, R. Sandhya, K. Laha, T. Jayakumar, *Int. J. Fatigue* **92**, 272 (2016)
- [43] J.H. Li, X.D. Wang, T.H. Ludwig, Y. Tsunekawa, L. Arnberg, J.Z. Jiangb, P. Schumachera, *Acta Mater.* **84**, 153 (2015)
- [44] S.K. Shaha, F. Czerwinski, W. Kasprzak, J. Friedman, D.L. Chen, *Int. J. Fatigue* **70**, 383 (2015)
- [45] C.H. Liu, J.S. Yang, P.P. Ma, Z.Y. Ma, L.H. Zhan, K.L. Chen, M.H. Huang, J.J. Li, Z.M. Li, *Int. J. Plast.* **134**, 102774 (2020)
- [46] Y.W. Jia, S.C. Wang, D. Shu, *J. Alloys Compd.* **821**, 153504 (2020)
- [47] D.Y. Wu, J. Kang, Z.H. Feng, R. Su, C.H. Liu, T. Li, L.S. Wang, *J. Alloys Compd.* **791**, 628 (2019)
- [48] K.Y. Wang, J. Xiang, R.D. Zhao, J.L. Bi, X.F. Wu, M.H. Chen, F.F. Wu, J. Eckert, *J. Alloys Compd.* **860**, 158421 (2021)
- [49] F. Mao, G.Y. Yan, Z.J. Xuan, Z.Q. Cao, T.M. Wang, *J. Alloys Compd.* **650**, 896 (2015)
- [50] R. Haghayeghi, G. Timelli, *Mater. Lett.* **283**, 128779 (2021)
- [51] B. Wang, P. Zhang, Q.Q. Duan, Z.J. Zhang, H.J. Yang, J.C. Pang, Y.Z. Tian, X.W. Li, Z.F. Zhang, *Mater. Sci. Eng. A* **711**, 533 (2018)